STRUCTURAL SCIENCE CRYSTAL ENGINEERING MATERIALS

ISSN 2052-5206

Charge density and electrostatic potential of hepatitis C anti-viral agent andrographolide: an experimental and theoretical study

Saravanan Manjula,[a] Chinnasamy Kalaiarasi,[a] Mysore S. Pavan,[b] Venkatesha R. Hathwar[c] and Poomani Kumaradhas[a]*

[a]Laboratory of Biocrystallography and Computational Molecular Biology Department of Physics, Periyar University, Salem, 636 011, India, [b]Solid State and Structural Chemistry Unit, Indian Institute of Science, Bangalore, 560 012, India, and [c]Department of Physics, Goa University, Goa 403 206, India. *Correspondence e-mail: kumaradhas@yahoo.com

Received 29 March 2018
Accepted 22 October 2018

Edited by P. Macchi, University of Bern, Switzerland

Keywords: andrographolide; electron density; hydrogen bonding; electrostatic potential; intermolecular interactions.

CCDC reference: 1554720

Supporting information: this article has supporting information at journals.iucr.org/b

Andrographolide (AGH) is a hepatitis C anti-viral agent which targets the host cell by covalently binding with the NF-κBreceptor. The experimental electron density distribution study of AGH has been carried out from high-resolution X-ray diffraction data collected at 110.2 (3) K. The unit-cell packing of AGH was stabilized by strong O—H···O and weak C—H···O types of intermolecular interactions. The dissociation energy of the strong hydrogen bond O2—H22···O1 is very high, 32 kJ mol^{-1}. The percentage occupancy of H···H interactions is found to be maximum (68.5%) when it comparing with the other types of interactions occurring in the AGH crystalline phase. The atomic valance index (V_{topo}) of the C16 atom is low compared with other carbon atoms; this shows that C16 could be the possible reactive location of the AGH molecule. All atoms in the OH groups have very low V_{topo} values; this indicates their role in strong hydrogen bonding interactions. The electrostatic potential (ESP) surface of AGH shows the polarization of the C16═C17 bond and ESP contour map shows several maxima at the vicinity of the C16 atom; these results strongly demonstrate that the C16 atom is the reactive location of the AGH molecule. The molecular covalent docking analysis of AGH with the NF-κB receptor has been performed and confirmed this result. The highly electronegative region around γ-butyrolactone can be helpful for initial alignment of the AGH molecule in NF-κB receptor active site. The atomic volumes of the hydrogen atoms which participate in the H···H interaction are found to be low.

1. Introduction

Hepatitis C is a virulent liver disease caused by hepatitis C virus (HCV) which affects 130–150 million people worldwide. The rapid replication rate of this virus and its vast genotype spectrum are the major hurdles for the development of vaccines and drugs for this disease (Rehermann & Nascimbeni, 2005; Gower *et al.*, 2014). The therapeutic options for chronic hepatitis C include two types, one of which adopts the combination of peglated interferon and ribavirin (Heim, 2013). The other is the combinational therapy of direct-acting antivirals (DAAs) such as sofosbuvir, simeprevir, boceprevir, declatasvir, paritaprevir, ombitasvir *etc.*, with or without interferon/ribavirin (Welzel *et al.*, 2014). Although these DAAs show potential activity against hepatitis C virus, there are some limitations that come into play. The potent action of DAAs is hampered by the emergence of HCV quasi-species and resistance mutations (De Francesco & Migliaccio, 2005). The evolution of new drugs against HCV with alternative

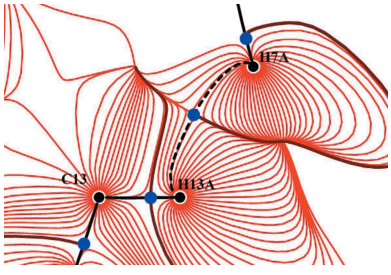

antiviral mechanisms which differ from those used by DAAs is urgently needed to handle the resistance mutation.

In the current scenario of HCV drug design, developing drug molecules with pan-genotypic nature and high barrier to resistance, is a prevailing challenge. In order to resolve this crisis, a detailed analysis of the molecular structure of the drug candidates at the bottom level is very essential. A detailed topological and electrostatic property analysis derived from the electron density distribution of the drug molecule is proven to be very useful in this case (Bouhmaida *et al.*, 2009; Yearley *et al.*, 2007; Grabowsky *et al.*, 2007, 2008) as the strength of drug-receptor interactions largely depends on the electron density distribution. The occurrence of intermolecular interactions in the crystalline unit cell and the biomolecular recognition are considered to have similar effects on the molecule at same dimensions (Grabowsky *et al.*, 2007, 2008). Thus, the polarization effects on the molecule due to crystalline and the drug-receptor interaction environment are comparable. Experimental electron density studies of several drug and bio-molecules, such as estrone (Zhurova, Matta *et al.*, 2006), 17α-estradiol·0.5H_2O (Zhurova *et al.*, 2009), genistein (Yearley *et al.*, 2007), paracetamol (Bouhmaida *et al.*, 2009), aziridine, oxirane, olefin (Grabowsky *et al.*, 2008), aspirin (Arputharaj *et al.*, 2012), isoniazid (Rajalakshmi, Hathwar *et al.*, 2014*b*), pyrazinamide (Rajalakshmi, Hathwar *et al.*, 2014*a*), ethionamide (Rajalakshmi, Pavan & Kumaradhas, 2014), 2-nitroimidazole (Kalaiarasi *et al.*, 2016), 16α,17β-estriol (Zhurova *et al.*, 2016), have been carried out and successfully established the importance of the electron density studies for understanding the nature of a molecule. The origin for the molecular recognition of a drug molecule is the structural and electrostatic complementarity with the receptor site amino-acid residues. This gives rise to polar interactions between positive and negative potential regions in the active site of a drug-receptor complex. The directional effects of these polar interactions can be effectively explained by the multipole model of experimental electron density (Muzet *et al.*, 2003). The electrostatic parameters of the drug molecule obtained from the electron density analysis help in the determination of its mode of interaction by marking the reactive locations of the molecule in the biological environment (Grabowsky *et al.*, 2007, 2008). This knowledge will provide the backbone information for structure- and ligand-based drug design methods.

Recently, andrographolide (AGH) (Scheme 1), the extract from the plant *Andrographis paniculata*, was reported to inhibit the replication of HCV by alternative and potentially proven antiviral mechanisms. It is reported to possess antiviral activity against HCV replication by the induction of haeme oxygenase-1 product biliverdin *via* the p38 kinase-mediated Nrf2 pathway (Lee *et al.*, 2014). AGH is a well known NF-κB inhibitor (Lim *et al.*, 2012; Xia *et al.*, 2004; Bao *et al.*, 2009; Chen *et al.*, 2011; Zhu *et al.*, 2013) which can act as an anti-inflammatory agent against carcinogenesis caused by HCV. Some previous studies (Chen *et al.*, 2013; Lee, Chen *et al.*, 2011; Lee, Tseng *et al.*, 2011; Lin *et al.*, 2013) reported that the suppression of NF-κB-mediated COX-2 expression inhibits the HCV replication. AGH inhibits NF-κB p50 by covalently conjugating the reduced cysteine 62 residue at the active site (Xia *et al.*, 2004). The covalent inhibition mechanism of AGH includes the nucleophilic attack at the exocyclic double bond of the AGH molecule due to the redox-regulated cysteine 62 residue followed by the Michael addition to form NF-κB p50 AGH covalent adduct (Nguyen *et al.*, 2015).

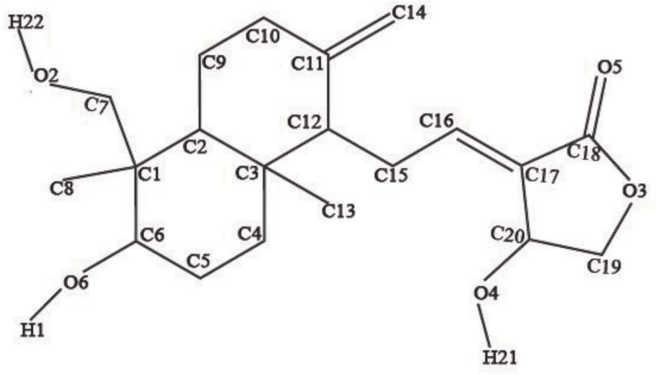

(I)

The electron density analysis of AGH will help to determine the behaviour of the drug molecule in the biological environment to inhibit the HCV replication. Accurate determination of the electrostatic properties of the AGH molecule from the experiment can disclose very valuable information about its reaction sites. This precise knowledge about the AGH molecule can help to find a new route to the design of new potent drugs against HCV. In the present study, the experimental electron density distribution of AGH is determined from the high-resolution X-ray diffraction data collected at the low temperature of 110.2 (3) K. The topological (electron density and Laplacian of electron density distribution) and electrostatic properties (atomic charges and electrostatic potential) are calculated for AGH. The strong and weak intermolecular interactions of the AGH molecule in the crystal are determined. The experimental results are compared with the corresponding theoretical solid-state and gas-phase quantum chemical calculations using density functional theory.

2. Experimental

2.1. X-ray intensity data collection and processing

Andrographolide in the powder form was purchased from Sigma Aldrich. The compound was crystallized from a chloroform and methanol solution by the slow evaporation technique. A good quality, plate-like single crystal was selected for the X-ray data collection for electron density analysis. The high-resolution X-ray diffraction intensity data were collected at 110.2 (3) K on an Xcalibur diffractometer (Rigaku Oxford Diffraction) using Mo $K\alpha$ radiation with an open-flow nitrogen cryostat (Cosier & Glazer, 1986). Of the 113 191 total reflections, 19 407 were found to be unique reflections and these were used in the refinement. The Lorentz, polarization and absorption corrections, and the

reflection intensity data integration and reduction were performed using *CryAlis PRO* (Agilent Technologies, 2012) software. The overall data set exhibits 99.8% completeness, a redundancy of 5.8 for the resolution $(\sin\theta/\lambda)_{max}$ = 1.08 Å^{-1} and an R_{int} value of 0.0518. The *SORTAV* (Blessing, 1987) program was used for averaging, sorting and merging the complete data.

2.2. Spherical atom refinement

The crystal structure of AGH was solved by the direct methods approach using *SHELXS97* (Sheldrick, 2008) in space group $P2_1$ and refined in the spherical atom approximation based on F^2 using *SHELXS97* of *WinGX* (Farrugia, 2012) software package. All non-hydrogen atoms were refined with anisotropic displacement parameters in the final refinement. The positions of all hydrogen atoms were located from the Fourier difference map and refined with isotropic displacement parameters. The experimental and spherical atom refinement details of the AGH molecule are presented in Table 1. The molecular displacement ellipsoid plot with atom numbering scheme (Fig. 1) was generated using *ORTEP3* (Farrugia, 1997). The unit-cell packing of AGH is generated from *PLATON* program (Spek, 2009) (see Fig. S1 in supporting information).

2.3. Multipole refinement

The electron density analysis of the AGH molecule was performed using the *XDLSM* module of the *XD2006* (Volkov *et al.*, 2006) software package. The multipole model refinement of the AGH molecule was carried out using the Hansen–Coppens multipole formalism (Hansen & Coppens, 1978). In this model, the expression of electron density, which is partitioned based on the population parameters, is given by

$$\rho_{atom}(r) = P_c\rho_{core}(r) + P_v\kappa^3\rho_{val}(\kappa r) + \sum_{l=0}^{l_{max}}\kappa'^3 R_l(\kappa' r)\sum_{m=0}^{l} P_{lm\pm}d_{lm\pm}(\vartheta,\varphi), \quad (1)$$

where P_c, P_v and P_{lm} are the core, valence and multipole population parameters, respectively; κ and κ' are the expansion–contraction of spherical and aspherical densities, respectively; $d_{lm\pm}$ is the normalized spherical harmonics and $R_l(\kappa' r)$ is the Slater-type radial function. The value of $\rho_{atom}(r)$ in equation (1).

For the multipole refinement, starting atom coordinates of the AGH molecule were taken from the spherical atom refinement and the anisotropic displacement parameters of H atoms obtained from *SHADE3* (Madsen, 2006) were used. Initially, the scale factor was refined; further, to obtain the accurate position of atoms, a high-order refinement $[(\sin\theta/\lambda)_{max} > 0.8$ Å] was performed; during this refinement, positions of H atoms were extended in the direction of C—H and O—H bonds using the neutron diffraction bond length values (Allen *et al.*, 1987). The Csp^3—H bond lengths of methyl, primary and secondary carbon atoms were fixed at 1.059, 1.092 and 1.099 Å, respectively. In the Csp^2—H-type bond, the distance of the H atom from the carbon atom was fixed as 1.077 Å. The distance of O—H bonds was fixed as 0.967 Å. During the refinement, the chemically equivalent atoms were constrained, which also reduces the number of refinement variables; however, these constraints were removed gradually at the final stage of refinement. During the refinement, all C and O atoms were treated up to octapole level (l = 3) and all H atoms up to dipole level (l = 2). The expansion/contraction parameter κ for H atoms was fixed as 1.2. The multipole parameters were refined using the following scheme: (i) scale factor, (ii) $P_v + \kappa$, (iii) $P_{lm} + \kappa'$, (iv) $xyz + U_{ij}$;

Table 1
Experimental details.

Crystal data	
Chemical formula	$C_{20}H_{30}O_5$
M_r	350.44
Crystal system, space group	Monoclinic, $P2_1$
Temperature (K)	110
a, b, c (Å)	6.5162 (1), 7.9477 (1), 17.9185 (2)
β (°)	97.023 (1)
V (Å^3)	921.02 (2)
Z	2
Radiation type	Mo $K\alpha$
μ (mm^{-1})	0.09
Crystal shape	Plate
Color	Colorless
Crystal size (mm)	0.43 × 0.28 × 0.23
Data collection	
Diffractometer	Xcalibur
Absorption correction	Analytical†
T_{min}, T_{max}	0.954, 0.982
No. of measured, independent and observed $[I > 2\sigma(I)]$ reflections	113 191, 19 407, 16 923
R_{int}	0.052
$(\sin\theta/\lambda)_{max}$ (Å^{-1})	1.080
Refinement	
$R[F^2 > 2\sigma(F^2)]$, $wR(F^2)$, S	0.034, 0.068, 1.53
No. of reflections	15 841
No. of parameters	255
$\Delta\rho_{max}$, $\Delta\rho_{min}$ (e Å^{-3})	0.27, −0.21

Computer programs: *CrysAlis RED* and *CrysAlis PRO* (Agilent Technologies, 2012), *SHELXS97* (Sheldrick, 2008), *XD2006* (Volkov *et al.*, 2006). † Analytical numeric absorption correction using a multifaceted crystal model based on expressions derived by Clark & Reid (1995). Empirical absorption correction using spherical harmonics, implemented in SCALE3 ABSPACK scaling algorithm.

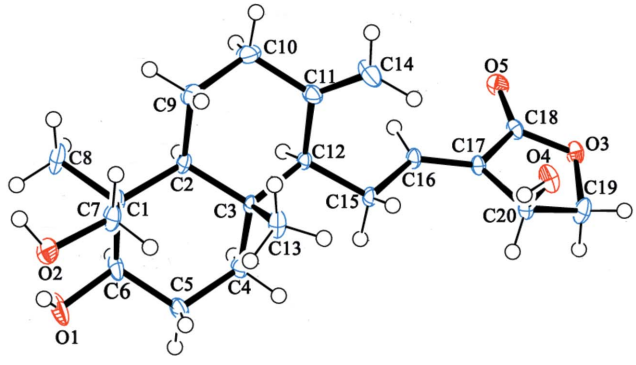

Figure 1
ORTEP view of the andrographolide molecule showing the atom numbering scheme. The displacement ellipsoids are drawn at the 50% probability level and H atoms are shown as spheres of arbitrary radii.

these refinement steps were used in a cyclic order until convergence. Further, in the final cycles of refinement, $P_v + \kappa + P_{lm} + \kappa'$ and $xyz + U_{ij}$ parameters were refined separately until convergence was achieved. A total electroneutrality constraint was maintained throughout the refinement. The imposed constraints were successively released and the final model was kept constraint free. The featureless residual density maps confirm the accuracy of the refinement and were obtained from *XDFOUR* and *XDFFT* (Volkov *et al.*, 2006) modules. The Hirshfeld rigid bond test was also performed; this shows slightly high values for bonds C17—C20 and C19—O3. Differences of mean-squares displacement amplitude values of all non-hydrogen bonds are presented in Table S4. Topological properties of electron density and the electrostatic properties of the AGH molecule and the intermolecular interactions are determined from the *XDPROP* (Volkov *et al.*, 2006) routine incorporated in the *XD2006* software. *TOPXD* (Volkov *et al.*, 2006) was used to calculate the AIM charges and the atomic volumes. The expansion/contraction parameters (κ, κ') of the multipole model are presented in Table S1.

3. Theoretical calculations

3.1. Solid-state DFT calculations

The DFT-based periodic quantum chemical calculation of AGH molecule was performed using *CRYSTAL09* (Dovesi *et al.*, 2005) software at B3LYP/6-31G**, B3LYP/TZVP, B3PW/6-31G** and B3PW/TZVP basis set (Hariharan & Pople, 1973). The input geometry for *CRYSTAL09* calculations was used from the final model of multipole refinement. Shrinking factors (IS1–IS3) along the reciprocal lattice vectors were set at 4 (30 *k*-points in the irreducible Brillouin zone). The truncation parameters were set as ITOL1 = ITOL2 = ITOL3 = ITOL4 = 6 and ITOL5 = 14. For better convergence, the level shifter value was set to 0.6 Hartree per cycle. Atomic position and displacement parameters were fixed to the values obtained from the experiment. The multipolar projection of theoretical structure factors was carried out using *XD2006* following the same steps used in the experimental multipole refinement until convergence. The results obtained from all basis sets are found to be good. The topological and electrostatic properties obtained from B3LYP/6-31G** are compared with those from the experimental model.

3.2. Gas-phase DFT calculations

A single point energy DFT calculation has been carried out for the AGH molecule obtained from the multipole model refinement using *Gaussian03* (Frisch *et al.*, 2005) software at the B3LYP/6-311G** level. Further, the wavefunction obtained from the above DFT (Parr & Yang, 1995) calculation was used to perform the electron density analysis using Bader's theory of atoms in molecules (Bader, 1990) implemented in *AIMPAC* (Frisch *et al.*, 2005) software. The experimentally derived electron density parameters obtained from multipole model are compared with the results of solid-state and gas-phase DFT calculations (Tables 2 and S5).

Table 2
Topological properties of electron density of andrographolide.

R_{ij} is the total bond path length. First line: experimental values; second line: *CRYSTAL09* calculations; third line: single point energy DFT calculations.

Bond	$\rho_{BCP}(r)$ (e Å^{-3})	$\nabla^2\rho_{BCP}(r)$ (e Å^{-5})	R_{ij} (Å)	Bond	$\rho_{BCP}(r)$ (e Å^{-3})	$\nabla^2\rho_{BCP}(r)$ (e Å^{-5})	R_{ij} (Å)
C1—C2	1.46 (2)	−6.9 (1)	1.571	C19—C20	1.65 (2)	−10.2 (1)	1.532
	1.49	−7.4	1.57		1.63	−9.5	1.531
	1.5	−10.7	1.578		1.65	−13.3	1.549
C1—C8	1.60 (2)	−9.5 (1)	1.542	C6—O1	1.62 (3)	−6.4 (1)	1.441
	1.56	−8.3	1.542		1.588	−5.3	1.441
	1.58	−12.1	1.547		1.632	−10.6	1.442
C3—C13	1.68 (2)	−10.9 (1)	1.535	C18—O3	2.25 (4)	−19.5 (2)	1.346
	1.58	−8.9	1.535		2.05	−17.3	1.346
	1.6	−12.4	1.542		1.94	−12.1	1.37
C10—C11	1.72 (2)	−11.3 (1)	1.508	C19—O3	1.61 (2)	−2.8 (1)	1.462
	1.66	−9.8	1.508		1.54	−4.6	1.46
	1.71	−14.5	1.509		1.66	−10.8	1.439
C11—C12	1.81 (3)	−12.6 (1)	1.51	C20—O4	1.78 (3)	−10.4 (1)	1.427
	1.69	−10.6	1.51		1.69	−6.6	1.426
	1.67	−13.7	1.521		1.69	−12.4	1.433
C11—C14	2.33 (3)	−23.4 (1)	1.338	C18—O5	2.91 (5)	−30.1 (3)	1.216
	2.22	−18.6	1.337		2.89	−33	1.216
	2.3	−23.9	1.334		2.86	−3.8	1.199
C16—C17	2.30 (3)	−23.6 (1)	1.339	O1—H1	2.22 (6)	−34.9 (5)	0.967
	2.29	−20.4	1.339		2.2	−24.1	0.967
	2.3	−24.2	1.335		2.48	−59.8	0.94
C17—C18	1.83 (3)	−13.7 (1)	1.476	O2—H22	2.32 (6)	−30.7 (4)	0.967
	1.79	−12.1	1.476		2.23	−23.8	0.967
	1.82	−16.2	1.485		2.46	−60.8	0.943
C17—C20	1.78 (2)	−11.8 (1)	1.507	O4—H21	2.23 (5)	−29.7 (3)	0.967
	1.69	−10.1	1.507		2.2	−24.2	0.967
	1.76	−15.3	1.502		2.48	−59.5	0.941

4. Results and discussion

4.1. Geometrical aspects

The room-temperature crystal structure of AGH has already been reported (Sambyal & Goswami, 1995). In the present study, the crystal structure of AGH is re-determined from low-temperature X-ray diffraction measurements to perform a charge density analysis. There is little difference in the unit-cell parameters of AGH crystals between the low-temperature and room-temperature studies. The low-temperature unit-cell parameters are slightly decreased, the maximum variation of unit-cell volume is 1.6%. However, this variation did not make any significant variation in the geometric parameters of the AGH molecule (Table S2); the values almost match those of the reported structure (Sambyal & Goswami, 1995). The unit-cell packing of the AGH molecule along the *b* axis is shown in Fig. S1a. The molecules in the unit cell are linked together by intermolecular interactions. The crystal structure was stabilized by O—H···O and C—H···O-type intermolecular interactions (see Desiraju & Steiner, 1999; Chopra *et al.*, 2010). Details of these interactions are presented in Table S3.

4.2. Hirshfeld and fingerprint analysis

In the drug-receptor complexes, knowledge of the interacting surface of the drug molecule is necessary to understand the intermolecular interactions between the drug and its

biological environment. The Hirshfeld surface provides an opportunity to visualize the interacting surface of a molecule in the crystalline phase. Fig. 2 shows the Hirshfeld surface view of the intermolecular interactions formed in the AGH crystal; the Hirshfeld surface is mapped with *Crystal Explorer* (Wolff *et al.*, 2012) software. The deep-red color on the surface illustrates the strong O—H···O and weak C—H···O interactions. These color indications in the molecular environment of the crystal space are very useful for identifying possible intermolecular interactions formed by the AGH molecule with its biological surrounding.

The two-dimensional fingerprint plot analysis is also performed from the information derived from the Hirshfeld surface. The fingerprint plots were generated by plotting the surface contact distances d_i against d_e. The data bin for all (d_i, d_e) pairs of the AGH molecule was created in the range 0–3 Å with d_i along the *x* axis and d_e along the *y* axis (Fig. S2a). The typical O···H contacts provide the shortest relative distance shown in Fig. S2b, which is indicated by two sharp spikes in the fingerprint plot. The common H···H contacts are shown in Fig. S2c. As the van der Waals radii of H atoms are much smaller than those of other atoms, the fingerprint plot covers the shortest distance. The relative percentages of occupancy of all interactions O···O < C···C < C···O < C···H < O···H < H···H in the AGH molecule are 0.6% < 1.0% < 1.2% < 2.0% < 26.7% < 68.5%, respectively.

4.3. Topological analysis of electron density

4.3.1. Electron density. The accuracy of the multipole model refinement is reflected by the featureless residual density map (Coppens, 1997). Fig. S3 shows the residual density maps of the AGH molecule drawn in two different planes. The topological properties of electron density (electron density, Laplacian, *etc.*) at the bond critical points (BCP) derived from the experiment, *CRYSTAL09* (Dovesi *et al.*, 2005; Hariharan & Pople, 1973) and gas-phase DFT calculations (B3LYP level of theory) (Frisch *et al.*, 2005; Parr & Yang, 1995; Cheeseman *et al.*, 1992) were compared with each other (Tables 2 and S5). The experimental electron density of the C18—O3—C19 region of the γ-butyrolactone ring shows a characteristic difference in the electron density between the C18—O3 and C19—O3 bonds. The electron density in the Csp^2—O bond C18—O3 [2.25 (4) e Å^{-3}] is found to be higher than in the Csp^3—O bond C19—O3 [1.61 (2) e Å^{-3}]; this difference has been attributed to the different bonding environments of atoms C18 (bonded with the carbonyl oxygen O5) and C19 (bonded with the sp^3 carbon C20). A similar trend is also observed in the corresponding values obtained from the theoretical solid-state and gas-phase calculations (Table 2) and such values also agree with the reported electron density distribution of C—O—C region found in the aspirin molecule (Arputharaj *et al.*, 2012). As expected, the carbonyl C18═O5 bond exhibits the highest value; the corresponding experimental electron density is 2.91 (5) e Å^{-3}. The experimental electron density values of C7—O2, C6—O1 and C20—O4 bonds are 1.71 (2), 1.62 (3) and 1.78 (3) e Å^{-3}, respectively; these densities are unequal and the difference is attributed to different bonding situations of C atoms. However, the low electron density value of C6—O1 is due to the association of the hydroxyl groups with the aliphatic ring carbon atom and the value also found to be less than the reported values of aromatic rings (Zhurova, Matta *et al.*, 2006; Holstein *et al.*, 2010), whereas this trend is opposite in the γ-butyrolactone ring. The electron density values of aliphatic Csp^3—H bonds range from 1.69 (5) to 1.97 (6) e Å^{-3} (Table S5); the experimental electron density values of C—H bonds in AGH are in agreement with those reported by Zhurova, Matta *et al.* (2006). The electron densities at the BCP of polar O—H bonds exhibit high values; the values range from 2.22 (6) to 2.32 (6) e Å^{-3}. Among the O—H bonds, the O2—H21 [2.32 (6) e Å^{-3}] bond is slightly high, such a trend is also found in the values calculated from solid-state theory (Table 2).

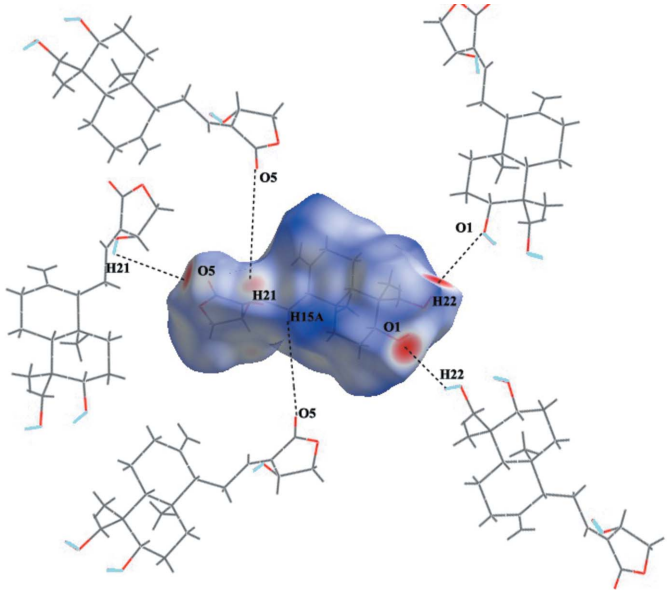

Figure 2
Hirshfeld surface of the andrographolide molecule mapped with surface d_{norm}. The pictorial representation shows the intermolecular interactions.

4.3.2. Laplacian of electron density. The Laplacian of electron density $\nabla^2\rho(r)$ at the BCP of chemical bonds determines the physical and chemical nature of atom–atom bonds in molecules (Bader, 1990). The (3,−1) type of BCP was obtained from the critical point search on all bonds of the AGH molecule. We have calculated the Laplacian of electron density $\nabla^2\rho(r)$ of AGH to understand its charge concentration and depletion (Tables 2 and S5). The experimental Laplacian of exocyclic bonds C11═C14 and C16═C17 are found to be almost equal at −23.4 (1) and −23.6 (1) e Å^{-5}, respectively. The charges of the carbonyl bond C18═O5 are highly concentrated, and the corresponding Laplacian value is −30.1 (3) e Å^{-5}. In the C18—O3—C19 bonding region of the γ-butyrolactone ring, the experimental Laplacian of bond C18—O3 is −19.5 (2) e Å^{-5}, whereas for the C19—O3 bond, the Laplacian is less negative [−2.8 (1) e Å^{-5}]; this latter value is found to be very small, which indicates that the charge

concentration has been reduced significantly and a similar trend is also observed in theory, where the corresponding value is −4.6 e Å^{-5}. This difference can be understood when we examine the eigenvalues λ_1, λ_2 and λ_3 at the BCP of the C19—O3 bond (Zhurova, Matta *et al.*, 2006; Zhurova *et al.*, 2009; Holstein *et al.*, 2010; Birkedal *et al.*, 2004; Volkov *et al.*, 2000; Volkov & Coppens, 2001) (Table S5). The charge concentration of hydroxyl C—O bonds C7—O2 [−7.6 (1) e Å^{-5}], C6—O1 [−6.4 (1) e Å^{-5}] and C20—O4 [−10.4 (1) e Å^{-5}] are found to be unequal; in particular, the charge concentration is less for the C—O bonds that are directly linked to the aliphatic ring (1). This variation may be attributed to the absence of a π-electron cloud of the ring, whereas this is found to be opposite in C—O bonds attached to the aromatic rings (Zhurova, Matta *et al.*, 2006; Zhurova *et al.*, 2009; Holstein *et al.*, 2010) of the molecules. All O—H bonds in the molecule exhibits a high degree of charge concentration and this can be confirmed from the high negative Laplacian values which range from −29.7 (3) to −34.9 (5) e Å^{-5}. However, there is a marked difference found among the Laplacian of these bonds and this may be due to the involvement of —OH groups in the hydrogen bonding interactions with the neighboring molecules. Notably, there is a significant difference found between the experimental and gas-phase Laplacian values of O—H bonds (Table 2). This difference may be due to the effect of the basis set used in the gas-phase calculations (Rajalakshmi, Hathwar *et al.*, 2014*a*,*b*; Zhurova, Matta *et al.*, 2006; Birkedal *et al.*, 2004; Volkov *et al.*, 2000). Fig. 3 displays the exact differences of Laplacian of electron density distribution of the molecule.

4.4. Topological bond order and atomic valence index

4.4.1. Topological bond order (n_{topo}). The strength of the chemical bonding between the atoms in a molecule can be determined by accurate topological bond order calculation. This method incorporates the topological properties of electron density $\rho_{BCP}(r)$ and the eigenvalue curvatures (λ_1, λ_2, λ_3) of Laplacian at the BCP which have been proven to give very reliable and precise bond order values (Howard & Lamarche, 2003; Tsirelson *et al.*, 2006, 2007; Zhurova, Matta *et al.*, 2006; Bartashevich *et al.*, 2011). The topological bond order of the AGH molecule has been calculated by the Howard and Lamarche expression (Howard & Lamarche, 2003),

$$n_{topo} = a + b\lambda_3 + c(\lambda_1 + \lambda_2) + d\rho_{BCP}. \qquad (2)$$

In the above equation (2), the values of coefficients used to calculate the bond orders for C—C bonds (Tsirelson *et al.*, 2007) are $a = -1.004$, $b = 0.634$, $c = 2.839$, $d = 17.633$; for C—O bonds $a = -0.668$, $b = -0.199$, $c = 0.567$, $d = 8.382$ (Tsirelson *et al.*, 2007); for C—H bonds $a = 0.128$, $b = 0.246$, $c = 0.480$, $d = 4.926$ (Zhurova, Stash *et al.*, 2006); for O—H bonds $a = 0$, $b = 0.11$, $c = -0.59$, $d = 5.27$ (Bartashevich *et al.*, 2011). These coefficients are obtained from the statistical treatment of equation (2). The bond order of C—C bonds ranges from 1.048 to 1.275. For the C11═C14 and C16═C17 bonds, the corresponding n_{topo} values are 1.595 and 1.457, respectively. The n_{topo} values of C—O bonds range from 0.718 to 1.156. The bond orders of C—H bonds range from 0.943 to 1.037. The n_{topo} values of O1—H1, O2—H22 and O4—H21 bonds are 0.529, 0.516 and 0.529, respectively. These values are found to be very low compared with values for other bonds; perhaps the low value of bond order may be due to the participation of O—H groups in intermolecular hydrogen bonding interactions (Zhurov & Pinkerton, 2014). The bond order of carbonyl C18═O5 (1.418) bond is found to be low; this is attributed to the participation of this bond in the intermolecular interactions. All calculated bond orders are found to be in agreement with the reported bond orders (Zhurov & Pinkerton, 2014; Tsirelson *et al.*, 2007, 2006). The selected topological bond order values of the AGH molecule calculated from the experiment, *CRYSTAL09* and single point energy calculations are presented in Tables 3 and S6.

4.4.2. Atomic valence index (V_{topo}). The atomic valence index V_{topo} is defined as the sum of bond orders of an atom in the molecule (Tsirelson *et al.*, 2006). The atoms in a molecule with unsaturated valence can be identified from the calculated

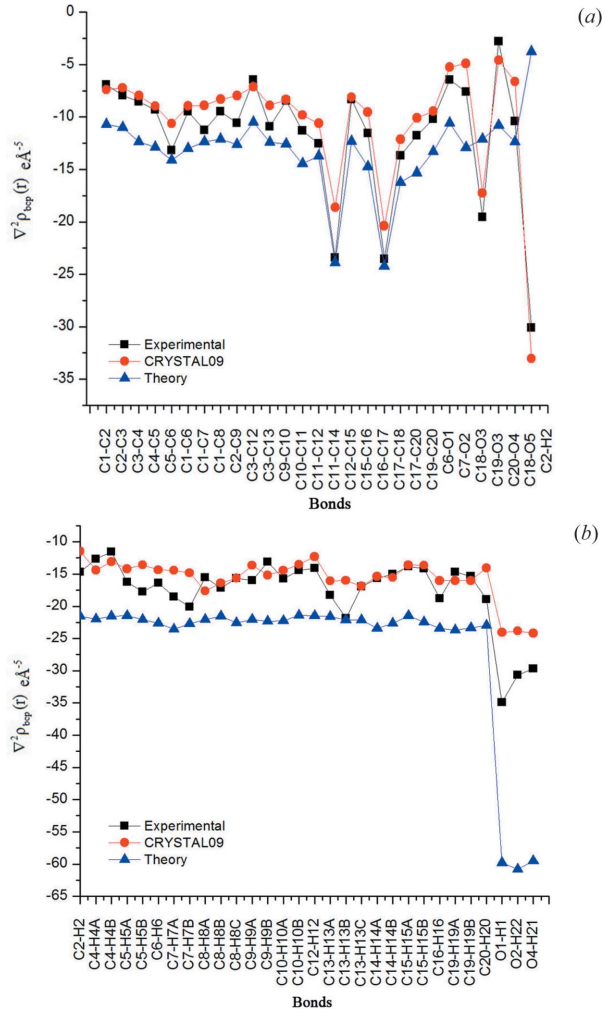

Figure 3
Comparison of Laplacian of electron density from experiment, *CRYSTAL09* and single point DFT calculations. (*a*) Bonds with nonhydrogen atoms and (*b*) bonds with hydrogen atoms.

Table 3
Topological bond order n_{topo} of andrographolide calculated from experiment, *CRYSTAL09* and quantum chemical calculations.

Bond	$n_{topo,expt}$	$n_{topo,\ theor\ (cryst09)}$	$n_{topo,\ theor\ (mol)}$
C1—C2	1.048	0.949	0.874
C2—C3	1.079	1.010	0.879
C3—C4	1.275	1.076	1.076
C4—C5	1.046	1.005	0.937
C5—C6	1.021	1.005	0.935
C1—C6	1.074	1.008	0.910
C1—C7	1.179	0.997	0.905
C1—C8	1.115	1.005	0.871
C2—C9	1.118	1.039	0.937
C3—C12	1.070	0.973	0.863
C3—C13	1.137	1.004	0.921
C9—C10	1.127	1.001	0.925
C10—C11	1.180	1.085	0.969
C11—C12	1.209	1.085	0.951
C11—C14	1.595	1.582	1.572
C12—C15	1.078	1.035	0.918
C15—C16	1.116	1.123	0.986
C16—C17	1.457	1.580	1.529
C17—C18	1.164	1.159	1.023
C17—C20	1.239	1.123	0.982
C19—C20	1.155	1.053	0.889
C6—O1	0.718	0.674	0.795
C7—O2	0.829	0.703	0.870
C18—O3	1.156	1.027	0.944
C19—O3	0.732	0.632	0.823
C20—O4	0.860	0.746	0.832
C18—O5	1.418	1.534	1.251
O1—H1	0.529	0.451	0.955
O2—H22	0.516	0.423	0.924
O4—H21	0.529	0.440	0.960

values of V_{topo} and this value helps to identify the highly reactive locations of the molecule (Tsirelson *et al.*, 2006, 2007). This approach is very useful to identify the reactive sites of a drug molecule present in the active site. The atom which has a lower valence index value than the other atoms of its kind in a molecule can undergo additional interactions most favorable to nucleophilic reactions (Tsirelson *et al.*, 2007). The experimental V_{topo} values of selected atoms of the AGH molecule have been calculated and are presented in Table 4. Among the values of all C atoms in the AGH molecule, the experimental V_{topo} values of the C16 atom are found to be very low ($V_{topo,expt}$ = 3.520). Similarly, all O—H group atoms (O1, O2 O4; H1, H22, H21) are also considered as more reactive atoms as their V_{topo} values are very low. And these atoms are also involved in strong inter- and intramolecular hydrogen bonding interactions in the crystal.

4.5. Electrostatic properties

4.5.1. Atomic charge and dipole moment. According to Bader (1990), atomic charges can be defined as the difference between the nuclear and electronic charges integrated over the atomic basins defined by zero-flux surfaces. The Bader's AIM charges of atoms in the AGH molecule were calculated using the *TOPXD* routine in the *XD2006* (Volkov *et al.*, 2006) program. As expected, the oxygen atoms O1, O2, O3, O4 and O5 carry highly negative charges, the values are −0.95 e, −1.09 e, −1.06 e, −1.06 e and −0.99 e, respectively. The

Table 4
Atomic valence index V_{topo} of andrographolide calculated from experiment.

Atom	$V_{topo,expt}$	Atom	$V_{topo,expt}$	Atom	$V_{topo,expt}$
C1	4.416	C11	3.984	O1	1.247
C2	4.220	C12	4.316	O2	1.345
C3	4.561	C13	4.153	O3	1.888
C4	4.305	C14	3.617	O4	1.389
C5	3.985	C15	4.139	O5	1.418
C6	3.802	C16	3.520	H1	0.529
C7	4.022	C17	3.860	H21	0.529
C8	4.133	C18	3.738	H22	0.516
C9	4.231	C19	3.948		
C10	4.301	C20	4.237		

charge of carbonyl carbon C18 is found to be highly positive (1.1 e) as it bonds with the highly negative O3 and O5 atoms. The C6, C7, C19 and C20 atoms also carry positive charges of 0.31 e, 0.37 e, 0.24 e and 0.37 e, respectively. The charges of H1, H21 and H22 atoms are more positive than the other H atoms which are bonded with the electronegative O1, O2 and O4 atoms. The atomic charges (monopole and AIM charges) of the atoms in AGH molecule calculated from multipole model refinement and AIM charges are presented in Table S8. The error Lagrangian is calculated from the relation $L_{err} = (\sum L^2{}_{\Omega}/N_{atoms})^{1/2}$, where L_{Ω} is the atomic integrated Lagrangian and has a value of 0.0074 a.u. The highest correlation coefficient in the least-squares model is 0.66. The dipole moment of the AGH molecule has been determined from multipole and quantum-derived in-crystal calculations to have values of 28.25 D and 18 D, respectively. The large variation of dipole moment may be attributed to the refinement strategy (Poulain-Paul *et al.*, 2012).

4.5.2. Electrostatic potential. The electrostatic potential (ESP) of molecules provides rich information about the binding ability of molecules with the neighboring molecules in solids as well as the binding of ligands in the active site of enzymes (Arputharaj *et al.*, 2012; Zhurova *et al.*, 2016, 2009; Zhurova, Matta *et al.*, 2006; Yearley *et al.*, 2007; Kalaiarasi *et al.*, 2016; Kumar & Dominiak, 2016; Rajalakshmi, Hathwar *et al.*, 2014*b*; Rajalakshmi, Pavan & Kumaradhas, 2014; Rajalakshmi, Hathwar *et al.*, 2014*a*; Dominiak *et al.*, 2007; Fournier *et al.*, 2009). Furthermore, in drug-receptor interactions, the ESP of a drug molecule allows molecular recognition in the biological environment (active site of receptor) to be predicted and, specifically, the reactive locations of the molecule to be identified; this information shows how the drug molecules interact with the receptor. Fig. 4(*a*) illustrates the experimental ESP isosurface (Hübschle & Luger, 2006) of the AGH molecule, showing the highly electronegative and -electropositive regions of the molecule. The vicinity of the C16 atom is surrounded by a positive ESP region, whereas the C17 atom is surrounded by a negative ESP region. Thus, in the ESP surface it is concluded that the C16═C17 bond is polarized. The C16═C17 bond is in conjugation with the C18═O5 bond and this makes the C16 atom more electrophilic and susceptible to nucleophilic attack. Thus ESP ensures that the C16═C17 bond is the possible reactive site of the AGH

molecule compared with any other region of the molecule. This prediction agrees well with the report (Nguyen *et al.*, 2015) which suggests that the nucleophilic attack is expected to take place in the vicinity of the C16 atom; after this the Micheal addition reaction occurs. In order to confirm this further, a contour ESP isosurface map was plotted (Fig. S5), in which several maxima (Grabowsky *et al.*, 2008) were found in the vicinity of the C16 atom; thus confirming that this is the possible reactive site location of the AGH molecule. Apart from this, the γ-butyrolactone moiety of the AGH molecule has a highly negative ESP region; presumably, it can form an interaction with the receptor. In view of this, it is expected that the γ-butyrolactone ring can play an important role in the alignment of the AGH molecule in the active site of the NF-κB receptor (Nguyen *et al.*, 2015) in order to undergo the nucleophilic attack.

In order to further validate this result, molecular docking was performed for AGH with the NF-κB p50 receptor. The AGH molecule was optimized using *Gaussian03* (Frisch *et al.*, 2005) software at B3LYP level of theory with 6-311G** basis set and docking was carried out with the *Schrodinger* (Zhu *et al.*, 2014) software package. The Cys62 residue of NF-κB p50 forms an irreversible covalent adduct with AGH at the C16 atom location facilitated by nucleophilic attack. Further, Val115 and Ile142 residues form O—H···O-type hydrogen bonding interactions with O1—H1 and O2—H22 groups with distances of 2.8 and 3.3 Å, respectively; and Ser66 forms NH···O-type hydrogen bonding interactions with O2 atom of AGH at a distance of 3.0 Å. The ESP isosurface of AGH in the active site environment with the intermolecular interactions is shown in Fig. 5. The docking study of AGH with NF-κB p50 receptor further confirms the results derived from the experimental ESP surface.

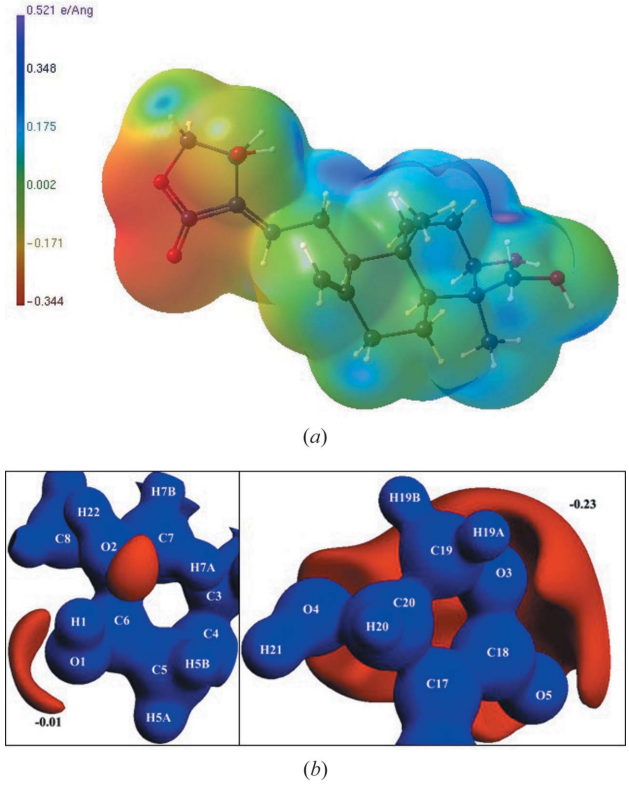

Figure 4
(*a*) MOLISO representation of the electrostatic potential surface of the andrographolide molecule. The iso value is 0.0067 e Å^{-3}. (*b*) Three-dimensional views of the ESP isosurface around the hydroxyl and carbonyl groups of the AGH molecule. Blue: positive ESP surface value is −0.6 e Å^{-1}, red: negative ESP surface values (left: −0.01 e Å^{-1}; right: −0.23 e Å^{-1}).

4.6. Topological properties of intermolecular interactions

4.6.1. Hydrogen bonding interactions. A critical point (CP) search was carried out on six noncovalent interactions and found a (3,−1)-type of CP for all interactions. We calculated their electron density and Laplacian values at the CP of these interactions (see Table 5). From these values, the kinetic energy density $G(r)$, potential energy density $V(r)$ and total energy density $H(r)$ were calculated (Bader, 1990; Abramov, 1997; Espinosa *et al.*, 1998). To understand the strength of these hydrogen bonding interactions, the bond dissociation energy D (Espinosa & Molins, 2000) of these interactions was calculated. The electron densities at the CP of all H···O of O—H···O hydrogen bonding interactions are: H1···O2 = 0.199, H21···O5^{i} = 0.135 and H22···O1^{i} = 0.207 e Å^{-3} [symmetry code (i) = $-x+1, y+\frac{1}{2}, -z$] and the corresponding Laplacian of electron density values are 4.0, 3.8 and 4.5 e Å^{-5}, respectively. Here, we found positive Laplacian $\nabla^2\rho(r) > 0$ with the conditions, $|V|/G < 2$ and $H(r) < 0$ of hydrogen bonding interactions confirm that these interactions are of partial covalent type (Espinosa & Molins, 2000; Desiraju, 1995; Keith *et al.*, 1996; Espinosa *et al.*, 2002; Gatti, 2005; Desiraju & Steiner, 1999; Koch & Popelier, 1995; Gu *et al.*, 1999; Stalke, 2011; Bader, 1998). Further, the electron density and Laplacian values of C—H···O interactions also

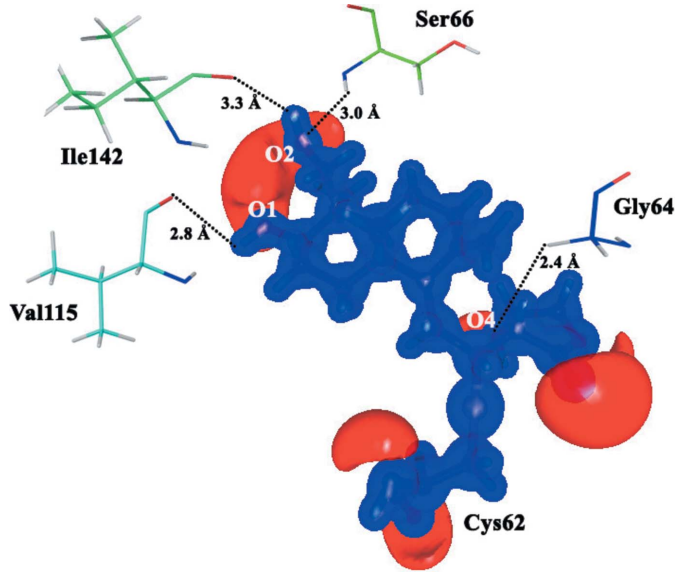

Figure 5
The ESP isosurface of the AGH molecule (isolated gas-phase) in the active site of NF-κB obtained from covalent docking (showing the intermolecular interactions). Blue: positive potential (+0.7 e Å^{-1}), red: negative potential (−0.07 e Å^{-1}).

Table 5
Topological properties of intra- and intermolecular interactions of the AGH molecule.

First line values are derived from experiment and second line values from *CRYSTAL09*. λ_1, λ_2, λ_3 are eigenvalues of the Hessian matrix, d_1, d_2 are the distance between BCP and each bonded atom; $G(r)$, $V(r)$ and $H(r)$ are the kinetic, potential and total energies, respectively; D is the dissociation energy.

Bond	$\rho_{BCP}(r)$ (e Å^{-3})	$\nabla^2\rho_{BCP}(r)$ (e Å^{-5})	λ_1 (e Å^{-5})	λ_2 (e Å^{-5})	λ_3 (e Å^{-5})	R_{ij} (Å)	d_1 (Å)	d_2 (Å)	$G(r)$ (a.u.)	$V(r)$ (a.u.)	$H(r)$ (a.u.)	D (kJ mol^{-1})
H1···O2	0.199	3.95	−1.00	−0.96	5.91	1.804	0.632	1.172	0.032	−0.022	0.010	28.9
	0.228	4.16	−1.23	−1.13	6.52	1.789	0.633	1.156	0.034	−0.025	0.009	32.8
H21···O5^{i}	0.135	3.79	−0.67	−0.64	5.10	1.844	0.621	1.224	0.028	−0.010	0.018	13.1
	0.169	3.59	−0.91	−0.89	5.39	1.843	0.650	1.193	0.028	−0.019	0.009	24.9
H22···O1^{ii}	0.207	4.49	−1.23	−1.03	6.75	1.742	0.598	1.145	0.036	−0.025	0.011	32.8
	0.233	4.43	−1.34	−1.28	7.05	1.742	0.611	1.132	0.036	−0.026	0.010	34.1
H8*B*···O2^{iii}	0.022	0.56	−0.07	−0.05	0.67	2.665	1.043	1.621	0.004	−0.002	0.002	2.6
	0.028	0.55	−0.09	−0.09	0.73	2.658	1.097	1.561	0.004	−0.002	0.002	2.6
H13*C*···O5^{i}	0.009	0.21	−0.04	−0.02	0.27	3.029	1.268	1.762	0.0015	−0.0008	0.0007	1.1
	0.017	0.34	−0.05	−0.04	0.43	2.876	1.211	1.665	0.0024	−0.0013	0.0011	1.7
H15*A*···O5^{i}	0.020	0.65	−0.06	−0.05	0.77	2.574	0.981	1.593	0.0046	−0.0024	0.0022	3.2
	0.035	0.66	−0.12	−0.11	0.89	2.573	1.065	1.508	0.0048	−0.0028	0.0020	3.6

Symmetry code: (i) $-x+1, y+\frac{1}{2}, -z$; (ii) $x+1, y, z$; (iii) $-x, \frac{1}{2}+y, -z$.

calculated, the values of H8*B*···O2^{i}, H13*C*···O5^{i} and H15*A*···O5^{i} interactions are 0.022, 0.009 and 0.02 e Å^{-3}, and 0.6, 0.2 and 0.7 e Å^{-5}, respectively. The positive value of Laplacian, $|V|/G < 1$ and $H(r) > 0$ of hydrogen bonding interactions reveals that these are closed-shell-type interactions (Gatti, 2005). On comparing the dissociation energies of O—H···O and C—H···O hydrogen bonds, it is noticeable that the O—H···O bonds are much stronger than the other interactions. Figs. S6 and S7 show the contour Laplacian and relief maps of the above-mentioned hydrogen bonding interactions. These maps display the alignment of lone-pair electrons present in the acceptor O atom towards the direction of the donor H atom in each of the hydrogen bonding interactions.

4.6.2. Hydrogen···hydrogen interactions. The H···H interactions are a special type of non-bonded or shared interaction, which favor the local stabilization of a molecule in the crystal environment (Zhurova, Matta *et al.*, 2006). Unlike the conventional hydrogen bonding and dihydrogen bonding interactions, the H···H interactions are neutral in nature and occur between two H atoms with similar charges and electronic environment (Matta *et al.*, 2003). These interactions are categorized as closed-shell interactions with low electron density and positive Laplacian at the CP (Matta, 2006). The intramolecular H···H interactions of the AGH molecule are presented in Table 6. The atomic volume of all atoms participating in the H···H interactions are found to be smaller, except H atoms H1, H13*C*, H21 and H22 which are involving strong (O—H···O) and weak C—H···O) hydrogen bonding interactions. In the H13*A*···H7*A* interactions, the volumes of both H13*A* and H7*A* atoms are found to be less

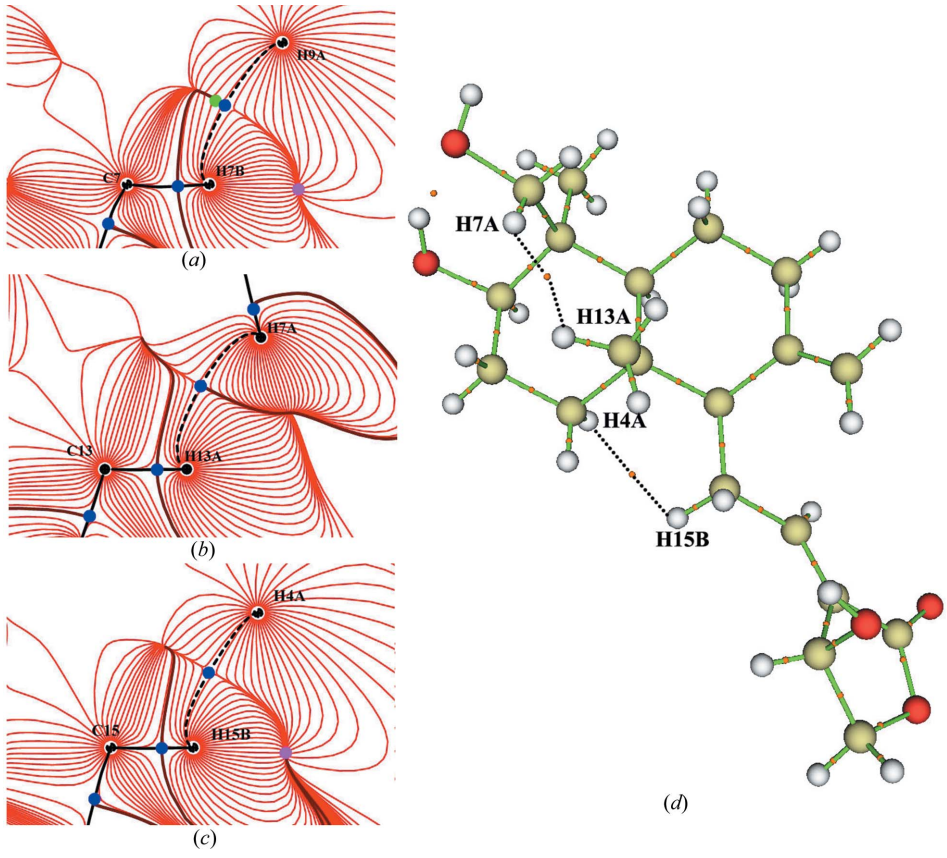

Figure 6
(*a*)–(*c*) Experimental electron density gradient line maps of H···H interactions and (*d*) a molecular map from theoretical calculation.

Table 6
Topological properties of intramolecular H···H bonding interactions of AGH molecule.

First line values are derived from experiment, second line values from *CRYSTAL09* and third line values from theory. λ_1, λ_2, λ_3 are eigenvalues of the Hessian matrix, d_1, d_2 are the distance between BCP and each bonded atom; $G(r)$, $V(r)$ and $H(r)$ are the kinetic, potential and total energies, respectively; D is the dissociation energy.

Bond	$\rho_{BCP}(r)$ (e Å^{-3})	$\nabla^2\rho_{BCP}(r)$ (e Å^{-5})	λ_1 (e Å^{-5})	λ_2 (e Å^{-5})	λ_3 (e Å^{-5})	R_{ij} (Å)	d_1 (Å)	d_2 (Å)	G(r) (a.u.)	V(r) (a.u.)	H(r) (a.u.)	D (kJ mol^{-1})
H13*A*···H7*A*	0.073	1.00	−0.35	−0.24	1.59	2.103	1.097	1.007	0.008	−0.005	0.003	6.6
	0.069	1.90	−0.75	−0.26	2.92	1.972	1.006	0.966	0.014	−0.008	0.006	10.5
	0.064	0.84	−0.21	−0.18	1.24	2.226	1.158	1.068	0.006	−0.004	0.002	5.3
H15*B*···H4*A*	0.075	1.29	−0.27	−0.21	1.78	2.078	1.033	1.045	0.009	−0.006	0.003	7.9
	–	–	–	–	–	–	–	–	–	–	–	–
	0.085	1.27	−0.27	−0.09	1.63	2.356	1.133	1.223	0.010	−0.006	0.004	7.9
H9*A*···H7*B*	0.065	1.07	−0.26	−0.11	1.44	2.212	1.136	1.076	0.008	−0.005	0.003	6.6
	0.169	1.75	−1.22	−0.42	3.40	2.221	1.013	1.208	0.015	−0.013	−0.002	17.1
	–	–	–	–	–	–	–	–	–	–	–	–

when compared to their counterparts and similar scenario is also found in the H15*B*···H4*A* interaction. The difference in the volume of H atoms also indicates the difference in strength of the H···H interactions (Zhurova, Matta *et al.*, 2006). The electron density gradient line maps of intramolecular H···H interactions of AGH molecule obtained from the experiment and the molecular map from theoretical calculation are shown in Fig. 6.

5. Conclusion

The topological and electrostatic properties of AGH molecule derived from the experiment are found to be in good agreement with the corresponding theoretical calculations. The O—H···O and C—H···O-type of intra- and intermolecular hydrogen bonding interactions found in the crystal explain well the nature of initial intermolecular interactions that can likely occur when AGH is present in the biological environment. The Hirshfeld surface analysis outlined the strong and weakly interacting surface of the AGH molecule where another molecule or more possibly the biomolecules come into contact and interact with the AGH molecule. Due to the absence of the π-electron cloud in the aliphatic rings of the AGH molecule, the electron density and Laplacian values at the BCP of C—O bonds are found to be less compared with the aromatic ring attached C—O bonds. The molecular recognition of AGH in the binding site should be mediated by the polar O—H bonds and highly electronegative oxygen atoms O3 and O5. The ability of the O—H bonds to participate in intermolecular interactions is demonstrated by the bond order calculation. The valence bond index is found to be very useful for identifying the C16 atom as the most reactive location in the AGH molecule. The dipole moment values obtained from multipole and quantum derived in-crystal calculations show large variation; this difference may arise due to the refinement strategy used in the multipole model refinement. The polarization difference found between C16 and C17 atoms in the contour map of the ESP surface clearly indicates atom C16 as the likely site for nucleophilic attack. The γ-butyrolactone ring is surrounded by high negative potential which can play a significant role in the initiation of nucleophilic attack when the AGH molecule is present at the appropriate position of the binding site. The intermolecular O—H···O interactions formed by AGH molecule in the crystalline phase are comparable with the interactions identified in AGH-NFκB p50 complex. Thus, the in-depth electronic level understanding obtained from the experimental electron density and electrostatic properties of AGH is helpful for predicting the possible interactions with amino acid residues present in the biological reactive sites. As AGH is already proven to be an inhibitor of HCV replication, the details about the drug-receptor intermolecular interactions derived from the present study will be helpful for the ligand- and structure- based drug design approaches of future anti-HCV agents which follow the same antiviral strategy as of AGH.

Acknowledgements

The authors thank Professor T. N. Guru Row for collecting the high-resolution X-ray intensity data and C-DAC, GARUDA supercomputing facility, Bangalore, for performing the theoretical calculations. The authors thank Schrodinger, Bangalore, for the use of the software for the covalent docking studies. There are no conflicts to declare.

References

Abramov, Y. A. (1997). *Acta Cryst.* A**53**, 264–272.
Agilent Technologies (2012). *CrysAlis PRO*. Version 1.171.37.34. and *CrysAlis RED*. Rigaku Oxford Diffraction, Yarnton, England.
Allen, F. H., Kennard, O., Watson, D. G., Brammer, L., Orpen, A. G. & Taylor, R. (1987). *J. Chem. Soc. Perkin Trans. 2*, p. S1.
Arputharaj, D. S., Hathwar, V. R., Guru Row, T. N. & Kumaradhas, P. (2012). *Cryst. Growth Des.* **12**, 4357–4366.
Bader, R. F. W. (1990). *Atoms in Molecules*. Oxford University Press.
Bader, R. F. W. (1998). *J. Phys. Chem. A*, **102**, 7314–7323.
Bao, Z., Guan, S., Cheng, C., Wu, S., Wong, S. H., Kemeny, D. M., Leung, B. P. & Wong, W. S. F. (2009). *Am. J. Respir. Crit. Care Med.* **179**, 657–665.
Bartashevich, E. V., Nikulov, D. K., Vener, M. V. & Tsirelson, V. G. (2011). *Comput. Theor. Chem.* **973**, 33–39.

Birkedal, H., Madsen, D., Mathiesen, R. H., Knudsen, K., Weber, H.-P., Pattison, P. & Schwarzenbach, D. (2004). *Acta Cryst.* A**60**, 371–381.

Blessing, R. H. (1987). *Crystallogr. Rev.* **1**, 3–58.

Bouhmaida, N., Bonhomme, F., Guillot, B., Jelsch, C. & Ghermani, N. E. (2009). *Acta Cryst.* B**65**, 363–374.

Cheeseman, J., Keith, T. A. & Bader, R. F. W. (1992). *AIMPAC* Program Package. McMaster University Press, Hamilton, ON, Canada

Chen, I., Khaki, L., Lindsey, J. C., Fry, C., Cousins, M. M., Siliciano, R. F., Violari, A., Palumbo, P. & Eshleman, S. H. (2013). *PLoS One*, **8**, 1–8.

Chen, H. W., Lin, A. H., Chu, H. C., Li, C. C., Tsai, C. W., Chao, C. Y., Wang, C. J., Lii, C. K. & Liu, K. L. (2011). *J. Nat. Prod.* **74**, 2408–2413.

Chopra, D., Guru Row, T. N., Arunan, E. & Klein, R. A. (2010). *J. Mol. Struct.* **964**, 126–133.

Clark, R. C. & Reid, J. S. (1995). *Acta Cryst.* A**51**, 887–897.

Coppens, P. (1997). *X-ray Charge Density and Chemical Bonding*. Oxford University Press.

Cosier, J. & Glazer, A. M. (1986). *J. Appl. Cryst.* **19**, 105–107.

De Francesco, R. & Migliaccio, G. (2005). *Nature*, **436**, 953–960.

Desiraju, G. R. (1995). *Angew. Chem. Int. Ed. Engl.* **34**, 2311–2327.

Desiraju, G. R. & Steiner, T. (1999). *The Weak Hydrogen Bonds in Structural Chemistry and Biology*. Oxford University Press.

Dominiak, P. M., Volkov, A., Li, X., Messerschmidt, M. & Coppens, P. (2007). *J. Chem. Theor. Comput.* **3**, 232–247.

Dovesi, R., Orlando, R., Civalleri, B., Roetti, C., Saunders, V. R. & Zicovich-Wilson, C. M. (2005). *Z. Kristallogr. Cryst. Mater.* **220**, 571–573.

Espinosa, E., Alkorta, I., Elguero, J. & Molins, E. (2002). *J. Chem. Phys.* **117**, 5529–5542.

Espinosa, E. & Molins, E. (2000). *J. Chem. Phys.* **113**, 5686–5694.

Espinosa, E., Molins, E. & Lecomte, C. (1998). *Chem. Phys. Lett.* **285**, 170–173.

Farrugia, L. J. (1997). *J. Appl. Cryst.* **30**, 565.

Farrugia, L. J. (2012). *J. Appl. Cryst.* **45**, 849–854.

Fournier, B., Bendeif, E. E., Guillot, B., Podjarny, A., Lecomte, C. & Jelsch, C. (2009). *J. Am. Chem. Soc.* **131**, 10929–10941.

Frisch, M. J. *et al.* (2005). *Gaussian03*. Gaussian Inc., Wallingford, CT, USA.

Gatti, C. (2005). *Z. Kristallogr. Cryst. Mater.* **220**, 399–457.

Gower, E., Estes, C., Blach, S., Razavi-Shearer, K. & Razavi, H. (2014). *J. Hepatol.* **61**, S45–S57.

Grabowsky, S., Pfeuffer, T., Chęcińska, L., Weber, M., Morgenroth, W., Luger, P. & Schirmeister, T. (2007). *Eur. J. Org. Chem.* pp. 2759–2768.

Grabowsky, S., Pfeuffer, T., Morgenroth, W., Paulmann, C., Schirmeister, T. & Luger, P. (2008). *Org. Biomol. Chem.* **6**, 2295.

Gu, Y., Kar, T. & Scheiner, S. (1999). *J. Am. Chem. Soc.* **121**, 9411–9422.

Hansen, N. K. & Coppens, P. (1978). *Acta Cryst.* A**34**, 909–921.

Hariharan, P. C. & Pople, J. A. (1973). *Theor. Chim. Acta*, **28**, 213–222.

Heim, M. H. (2013). *Nat. Rev. Immunol.* **13**, 535–542.

Holstein, J. J., Luger, P., Kalinowski, R., Mebs, S., Paulman, C. & Dittrich, B. (2010). *Acta Cryst.* B**66**, 568–577.

Howard, S. T. & Lamarche, O. (2003). *J. Phys. Org. Chem.* **16**, 133–141.

Hübschle, C. B. & Luger, P. (2006). *J. Appl. Cryst.* **39**, 901–904.

Kalaiarasi, C., Pavan, M. S. & Kumaradhas, P. (2016). *Acta Cryst.* B**72**, 775–786.

Keith, T. A., Bader, R. F. W. & Aray, Y. (1996). *Int. J. Quantum Chem.* **57**, 183–198.

Koch, U. & Popelier, P. L. A. (1995). *J. Phys. Chem.* **99**, 9747–9754.

Kumar, P. & Dominiak, P. M. (2016). *Biophys. J.* **110**, 380.

Lee, J. C., Chen, W. C., Wu, S. F., Tseng, C., Chiou, C., Chang, F., Hsu, S. & Wu, Y. (2011). *Antiviral Res.* **89**, 35–42.

Lee, J.-C., Tseng, C.-k., Wu, S.-F., Chang, F.-R., Chiu, C.-C. & Wu, Y.-C. (2011). *J. Viral Hepat.* **18**, e315–e324.

Lee, J.-C., Tseng, C.-K., Young, K.-C, Sun, H. Y., Wang, S. W., Chen, W. C., Lin, C. K. & Wu, Y. H. (2014). *Br. J. Pharmacol.* **171**, 237–252.

Lim, J. C. W., Chan, T. K., Ng, D. S., Sagineedu, S. R., Stanslas, J. & Wong, W. F. (2012). *Clin. Exp. Pharmacol. Physiol.* **39**, 300–310.

Lin, Y.-T., Wu, Y.-H., Tseng, C.-K., Lin, C.-K., Chen, W.-C., Hsu, Y.-C. & Lee, J.-C. (2013). *PLoS One*, **8**, e54466.

Madsen, A. Ø. (2006). *J. Appl. Cryst.* **39**, 757–758.

Matta, C. F. (2006). *Challenges and Advances in Computational Chemistry and Physics Series*, pp. 337–376. Springer.

Matta, C. F., Hernández-Trujillo, J., Tang, T.-H. & Bader, R. F. W. (2003). *Chem. Eur. J.* **9**, 1940–1951.

Muzet, N., Guillot, B., Jelsch, C., Howard, E. & Lecomte, C. (2003). *PNAS*, **100**, 8742–8747.

Nguyen, V. S., Loh, X. Y., Wijaya, H., Wang, J., Lin, Q., Lam, Y., Wong, W. F. & Mok, Y. K. (2015). *J. Nat. Prod.* **78**, 208–217.

Parr, R. G. & Yang, W. (1995). *Density Functional Theory of Atoms and Molecules*. London: Oxford University Press.

Poulain-Paul, A., Nassour, A., Jelsch, C., Guillot, B., Kubicki, M. & Lecomte, C. (2012). *Acta Cryst.* A**68**, 715–728.

Rajalakshmi, G., Hathwar, V. R. & Kumaradhas, P. (2014*a*). *Acta Cryst.* B**70**, 568–579.

Rajalakshmi, G., Hathwar, V. R. & Kumaradhas, P. (2014*b*). *Acta Cryst.* B**70**, 331–341.

Rajalakshmi, G., Pavan, M. S. & Kumaradhas, P. (2014). *RSC Adv.* **4**, 57823–57833.

Rehermann, B. & Nascimbeni, M. (2005). *Nat. Rev. Immunol.* **5**, 215–229.

Sambyal, V. S. & Goswami, K. N. (1995). *Cryst. Res. Technol.* **30**, 629–636.

Sheldrick, G. M. (2008). *Acta Cryst.* A**64**, 112–122.

Spek, A. L. (2009). *Acta Cryst.* D**65**, 148–155.

Stalke, D. (2011). *Chem. Eur. J.* **17**, 9264–9278.

Tsirelson, V. G., Bartashevich, E. V., Stash, A. I. & Potemkin, V. A. (2007). *Acta Cryst.* B**63**, 142–150.

Tsirelson, V. G., Stash, A. I., Potemkin, V. A., Rykounov, A. A., Shutalev, A. D., Zhurova, E. A., Zhurov, V. V., Pinkerton, A. A., Gurskaya, G. V. & Zavodnik, V. E. (2006). *Acta Cryst.* B**62**, 676–688.

Volkov, A., Abramov, Y., Coppens, P. & Gatti, C. (2000). *Acta Cryst.* A**56**, 332–339.

Volkov, A. & Coppens, P. (2001). *Acta Cryst.* A**57**, 395–405.

Volkov, A., Macchi, P., Farrugia, L., Gatti, C., Mallinson, P., Richter, T. & Koritsanszky, T. (2006). *XD2006*, Version 5.33. University at Buffalo, State University of New York, NY, USA, University of Milano, Italy, University of Glasgow, UK, CNRISTM, Milano, Italy, Middle Tennessee State University, TN, USA.

Welzel, T. M., Dultz, G. & Zeuzem, S. (2014). *J. Hepatol.* **61**, S98–S107.

Wolff, S. K., Grimwood, D. J., McKinnon, J. J., Jayatilaka, D. & Spackman, M. A. (2007). *Crystal Explorer 3.0*. University of Western Australia, Perth, Australia.

Xia, Y.-F., Ye, B.-Q., Li, Y.-D., Wang, J.-G., He, X.-J., Lin, X., Yao, X., Ma, D., Slungaard, A., Hebbel, R. P., Key, N. S. & Geng, J.-G. (2004). *J. Immunol.* **173**, 4207–4217.

Yearley, E. J., Zhurova, E. A., Zhurov, V. V. & Pinkerton, A. A. (2007). *J. Am. Chem. Soc.* **129**, 15013–15021.

Zhu, K., Borrelli, K. W., Greenwood, J. R., Day, T., Abel, R., Farid, R. S. & Harder, E. (2014). *J. Chem. Inf. Model.* **54**, 1932–1940.

Zhu, T., Wang, D., Zhang, W., Liao, X., Guan, X., Bo, H., Sun, J., Huang, N., He, J., Zhang, Y., Tong, J. & Li, C. (2013). *PLoS One*, **8**, e56407.

Zhurov, V. V. & Pinkerton, A. A. (2014). *Cryst. Growth Des.* **14**, 5685–5691.

Zhurova, E., Matta, C. F., Wu, N., Zhurov, V. V. & Pinkerton, A. A. (2006). *J. Am. Chem. Soc.* **128**, 8849–8861.
Zhurova, E. A., Stash, A. I., Tsirelson, V. G., Zhurov, V. V., Bartashevich, E. V., Potemkin, V. A. & Pinkerton, A. A. (2006). *J. Am. Chem. Soc.* **128**, 14728–14734.
Zhurova, E. A., Zhurov, V. V., Chopra, D., Stash, A. I. & Pinkerton, A. A. (2009). *J. Am. Chem. Soc.* **131**, 17260–17269.
Zhurova, E. A., Zhurov, V. V., Kumaradhas, P., Cenedese, S. & Pinkerton, A. A. (2016). *J. Phys. Chem. B*, **120**, 8882–8891.